

The Active Corona of HD 35850 (F8 V)

Marc Gagné, Jeff A. Valenti, and Jeffrey L. Linsky

JILA, University of Colorado and NIST, Boulder, CO 80309-0440

Gianpiero Tagliaferri and Stefano Covino

Osservatorio Astronomico di Brera, via E. Bianchi 46, I-22055 Merate, Italia

and

Manuel Güdel

Paul Scherrer Institute, CH-5232, Villigen PSI, Switzerland

ABSTRACT

We present *Extreme Ultraviolet Explorer* spectroscopy and photometry of the nearby F8 V star HD 35850 (HR 1817). The *EUVE* short-wavelength 75–175 Å and medium-wavelength 160–365 Å spectra reveal 28 emission lines from Fe IX and Fe XV to Fe XXIV. The Fe XXI $\lambda\lambda$ 102, 129 ratio yields an upper limit for the coronal electron density, $\log n_e < 11.6 \text{ cm}^{-3}$. The *EUVE* SW spectrum shows a small but clearly detectable continuum. The 75–150 Å line-to-continuum ratio indicates approximately solar Fe abundances, with $0.8 < Z < 1.6$ (90% confidence interval). Upper limits have been derived for a dozen high-emissivity Fe X through Fe XIV lines. The resulting EM distribution is characterized by two broad temperature components at $\log T$ of 6.8 and 7.4. Over the course of the 1-week observation, large-amplitude, long-duration flares were not seen in the *EUVE* Deep Survey light curve, though the light curve does show signs of persistent, low-level flaring, and possible rotational modulation.

The *EUVE* spectra have been compared with non-simultaneous *ASCA* SIS spectra of HD 35850 obtained in 1995. The SPEX DEM analysis of the SIS spectrum indicate the same temperature distribution as the *EUVE* DEM analysis. However, the SIS spectra suggest sub-solar abundances, $0.34 < Z < 0.81$. Although some of the discrepancy may be the result of incomplete X-ray line lists, we cannot explain the disagreement between the *EUVE* line-to-continuum ratio and the *ASCA*-derived Fe abundance.

The X-ray surface flux on HD 35850 is comparable to that of cooler dwarfs of comparable age and rotation like EK Draconis (G0 V) and AB Doradus (K1 V). Given its youth ($t \approx 100 \text{ Myr}$), its rapid rotation ($v \sin i \approx 50 \text{ km s}^{-1}$), and its high X-ray activity ($L_X \approx 1.5 \times 10^{30} \text{ ergs s}^{-1}$), HD 35850 may represent an activity extremum for single, main-sequence F-type stars. The variability and EM distribution can be reconstructed using the continuous flaring model of Güdel provided that the flare distribution has a power-law index $\alpha \approx 1.8$. Similar results obtained for other young

solar analogs suggest that continuous flaring is a viable coronal heating mechanism on rapidly rotating, late-type, main-sequence stars.

Subject headings: stars: individual (HD 35850) – stars: coronae – stars: late-type – stars: rotation – X-Rays: stars – ultraviolet: stars

1. Introduction

By analogy to the Sun, magnetic heating in the chromospheres, transition regions, and coronae of late-type stars is observed as cooling in the Balmer lines, the Ca II lines, and in UV, FUV, EUV, and soft X-ray continuum and line emission. Results from the Mt. Wilson Ca II H and K survey of single lower main-sequence field stars has provided compelling evidence of Solar-like chromospheric active regions, activity cycles, differential rotation, and occasional Maunder minima in mid-F to early-M stars (e.g., Noyes et al. 1984; Baliunas et al. 1996; Gray & Baliunas 1997; Baliunas et al. 1995).

Coronal heating and magnetic dynamos on the Sun and in stars have been discussed extensively in the literature (cf. Haisch & Schmitt 1996). The various flares, microflares, nanoflares, and brightenings observed on the Sun are thought to be manifestations of current sheet reconnection and much of the coronal heating debate is focussed on whether or not these transient events can account for the radiative output of the solar corona (e.g., Oreshina & Somov 1998). While both continuous (e.g., MHD waves) and stochastic (nanoflaring) processes probably contribute to magnetic coronal heating, the dominant process has yet to be identified.

Empirically, coronal emission on active, cool, main-sequence stars is similar to flare emission from solar active regions. For example, Benz & Güdel (1994) find a similar correlation between X-ray luminosity and non-thermal continuum radio luminosity for solar flares and active stars. On the Sun, mildly relativistic electrons accelerated along coronal magnetic field lines produce gyrosynchrotron radio emission. The presence of persistent but variable nonthermal radio emission from cool stars indicates a continual replenishment of the relativistic electron population while a correlation between coronal and radio emissions suggests a causal relationship between electron acceleration in magnetically confined loops and coronal heating. In the 50,000–200,000 K regime, further evidence of continual flaring comes from the broad emission-line components seen in high-resolution UV spectra of active dwarfs and RS CVn binaries. Because the broad-component line widths are 2–4 times the thermal width and because the broad components are blue-shifted relative to the narrow components, Wood et al. (1996) suggest that the broad components are produced by transition-region explosive events.

Two well-studied examples of extreme main-sequence magnetic activity are the Pleiades-age, rapid rotators AB Doradus (K0 V) and EK Draconis (G0 V). Spectro-polarimetric monitoring of AB Dor shows long-lived, cool magnetic spots and latitudinal differential rotation (Donati &

Collier Cameron 1997). *ROSAT* PSPC soft X-ray photometry of AB Dor (Kürster et al. 1997) shows rotationally modulated flare and quiescent emission with the same phase and period (12.4 h) as the photospheric spots. *ASCA* and *EUVE* spectra of AB Dor and EK Dra indicate coronal emission-measure distributions, $\text{Em}(T)$, with peaks at 5–8 MK and 20–30 MK (Mewe et al. 1996; Güdel et al. 1997).

The 5–8 MK component has been observed in other moderately active coronal sources, most notably Capella (Brickhouse, Raymond, & Smith 1995). As has been pointed out by Gehrels & Williams (1993), optically thin plasma tends to accumulate at temperatures where the cooling curve $\Omega(T)$ has a positive slope. This is a manifestation of the Parker (1953) & Field (1965) instability: when $\frac{d\Omega(T)}{dT} > 0$, plasma cools more efficiently at slightly higher temperatures and less efficiently at slightly lower temperatures. At temperatures where $\frac{d\Omega(T)}{dT} < 0$, plasma quickly cools to lower temperatures. For solar-abundance plasmas, $\frac{d\Omega(T)}{dT} > 0$ in the ranges 0.7–1.2 MK, 4.5–7 MK, and above 21 MK. Thus, the shape of the cooling curve explains the dip from 2–4 MK and from 9–20 MK seen in many EM distributions and provides some physical justification for two- and three-temperature coronal models. The temperature of the hot component and the relative amount of hot emission measure must reflect a balance between magnetic heating and radiative cooling. For stars with significant emission measure above 20 MK, some mechanism must be super-heating the coronal plasma at fairly regular intervals.

For three active, solar-mass stars observed with the *ASCA* SIS (EK Dra, HN Pegasii, and κ^1 Ceti in order of decreasing activity), Güdel (1997) has modeled $\text{Em}(T)$ by assuming X-rays are produced by an ensemble of flaring and cooling loops. The Güdel (1997) model is a modification of the solar nanoflare model proposed by Kopp & Poletto (1993). While the *ASCA* data cannot constrain many model parameters (number of loops, loop dimension, and mean magnetic field strength), the models can only reproduce the observed $\text{Em}(T)$ provided that the power-law distribution of flare and microflare energies is $\alpha \approx 2$. High S/N spectra of other active dwarfs are needed to test the viability of continuous flaring and to establish the importance of this mechanism as a function of rotation rate and effective temperature.

In this paper, we present EUV and X-ray spectroscopy of HD 35850 = HR 1817 (F8 V). HD 35850 was detected serendipitously with *EXOSAT* (Cutispoto et al. 1991) and follow-up optical spectroscopy has established it as a nearby, single, solar-metallicity Pleiades-age ($t \approx 10^8$ yr), rapid rotator (Tagliaferri et al. 1994). We are particularly interested in HD 35850 because it is probably in the extreme state of magnetic activity for single, main-sequence F stars. There is considerable interest in probing the magnetic dynamo in F stars because they possess relatively shallow convection zones. Kim & Demarque estimate that, in a 10^7 yr-old $1.1\text{--}1.2M_{\odot}$ star like HD 35850, the convective turnover time is $\tau_c \approx 20$ d. In a young $1.0M_{\odot}$ star like EK Dra, $\tau_c \approx 40$ d.

2. Observations and Data Analysis

HD 35850 was observed by the *Extreme Ultraviolet Explorer* from 1995 October 23 08:17:07 UT to 1995 October 30 07:20:34 UT. The *EUVE* Deep Survey/Spectrometer consists of three aligned grazing-incidence telescopes. The telescope beams are intercepted by short-, medium-, and long-wavelength reflection gratings and detected with microchannel-plate detectors (SW, MW, and LW, respectively). The undispersed portions of the three beams are focussed onto the Deep Survey microchannel-plate detector, DS. This way, *EUVE* obtains simultaneous, time-resolved 75–120 Å broad-band photometry and 70–160 Å, 170–370 Å, and 300–525 Å medium-resolution spectra (cf. Haisch, Bowyer, & Malina 1993). In support of this *EUVE* observing program, Ca II HK spectra were obtained on 1996 October 2–12. HD 35850 was observed with the *ASCA* SIS and GIS for ~ 18 ks on 1995 March 12. The reduction and analysis of these data are described below.

2.1. *EUVE* Deep Survey Data

The *EUVE* Deep Survey/Spectrometer records photon events whenever the source is visible by the satellite, including times when the satellite is passing through the South Atlantic Anomaly (SAA). These SAA passages are characterized by increased background levels which lead to significant and poorly characterized loss of telemetry, nicknamed “primbsching”. Correcting for earth occultations, the on-source time was ~ 203 ks. Correcting for instrument and telemetry dead times, the net exposure time was ~ 198 ks.

The Deep Survey (DS) events were screened at various count-rate and primbsch-correction thresholds. Light curves were generated with bin times ranging from 100 to 2000 s. Source events were extracted from a 25 pixel radius circle centered on the PSF centroid. Background events were extracted from an annulus with inner and outer radii of 37 and 67 pixels, respectively. In Figure 1, we show the background-subtracted, dead-time and primbsch-corrected 75–120 Å DS light curve for HD 35850 using 1000 s bins and including times when primbsching (monitor Det7Q1dpc) was below 25%.

The mean DS background-corrected count rate of HD 35850 is $0.20 \text{ counts s}^{-1}$. No large flares are evident in the DS light curve: the variability amplitude is approximately 100% and the most significant deviation from the mean count rate is a 5σ peak near MJD 18.45. The light curve, however, shows small to moderate flares throughout the observation. At least 7 events have a peak count rate 3σ above the apparent “quiescent” level of $0.20 \text{ counts s}^{-1}$. To test the hypothesis that the observed counts come from a non-variable source, we have determined the cumulative distribution function of the unbinned photon arrival times for the observed data and for simulated data from a constant, $0.2 \text{ counts s}^{-1}$ source. A two-sample Kolmogorov-Smirnov test statistic (Feigelson & Babu 1992) was calculated using the observed and simulated distributions; the probability that the two data sets were drawn from the same parent population is low ($P \leq 10^{-9}$). We conclude that the DS light curve exhibits significant variability.

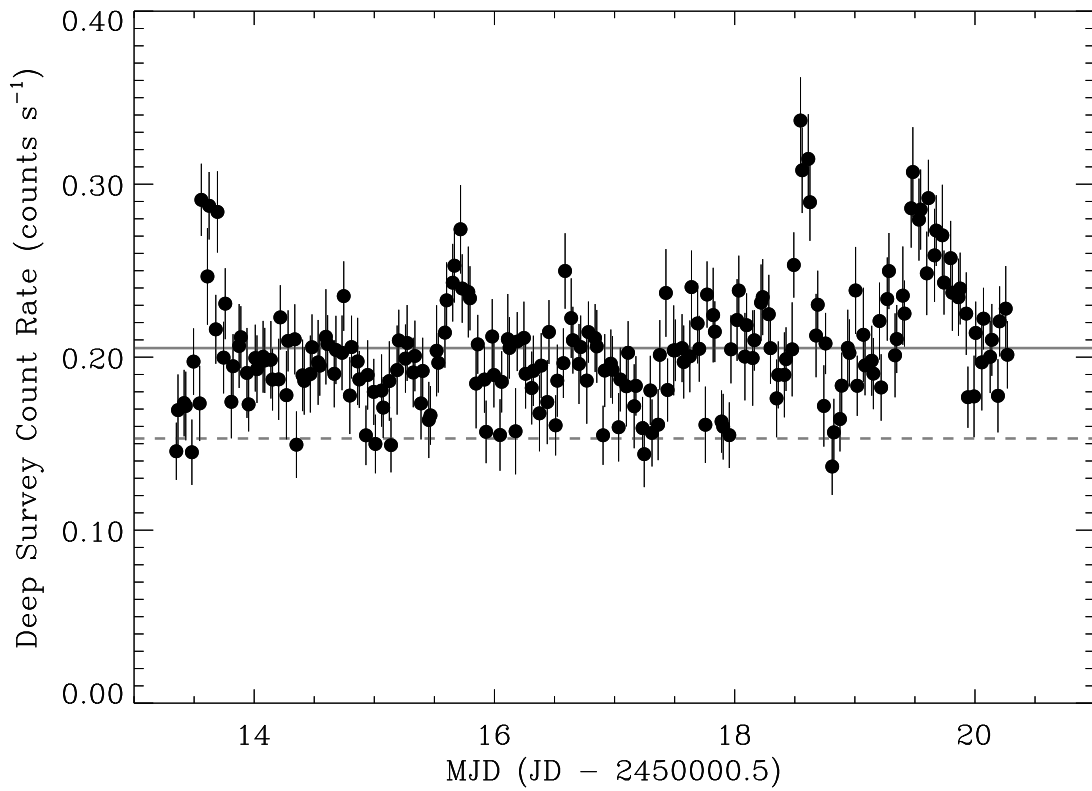


Fig. 1.— EUVE Deep Survey light curve (~ 950 s bins) of HD 35850 obtained 1995 October 23–30. The solid gray line indicates the mean DS count rate and the dashed gray line shows the estimated activity level during the ASCA observation in 1995 March.

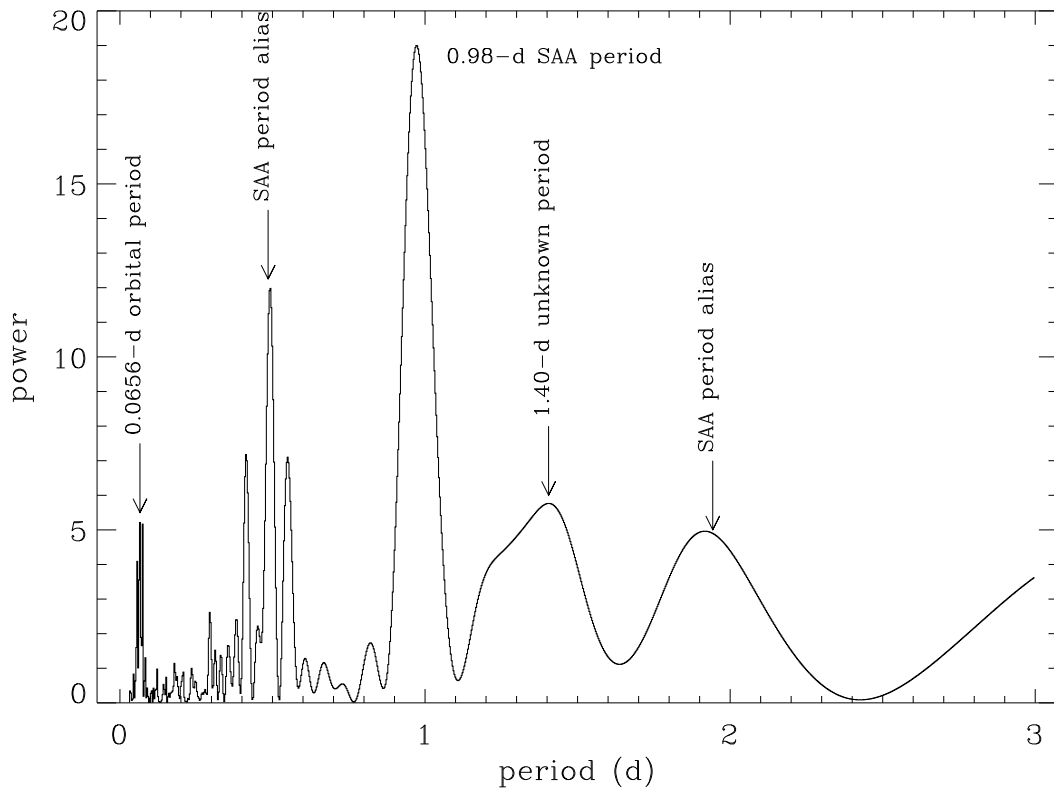


Fig. 2.— Scargle discrete Fourier transform for the binned DS light curve in Fig. 1. The power spectrum indicates significant power at 0.0656 d, 0.98-d, and its aliases. These periods are associated with satellite SAA passages. The only peak which cannot be assigned to systematic effects occurs near 1.40 d.

We have used the binned DS light curve to compute the discrete Fourier transform (Scargle 1989), shown in Figure 2. There is significant power around 0.98 d and its aliases. For HD 35850, $v \sin i \approx 50 \text{ km s}^{-1}$ and $R_* \approx 1.18 R_\odot$ implies $P_{\text{rot}}/\sin i \approx 1.1 \text{ d}$, consistent with the 0.98-d period. However, Halpern & Marshall (1996) report that 0.98 d is a beat period associated with the satellite’s passage through the SAA. For example, during the HD 35850 observation, the Det7Q1dpc monitor shows strong periodic signals at 0.984 d and at 0.0656 d. Similar periods have been seen in other primbsch-corrected light curves (Marshall 1998, private communication). We thus conclude that some or all of the 0.98-d signal seen in the DS light curve results from SAA passages. We note that the only period seen in HD 35850’s power spectrum that *cannot* be attributed to primbsching is at 1.40 d. Until further observations can be carried out, we tentatively identify 1.40 d as the rotation period of HD 35850 (see §2.2).

2.2. McMath-Pierce Optical Spectroscopy

Medium-resolution Ca II HK spectra were obtained with the Solar-Stellar Spectrograph at the National Solar Observatory’s McMath-Pierce Telescope on 1996 October 2–12, ten days before the *EUVE* observation. The spectra around HK are typical of active, late-type dwarfs, with broad absorption troughs and bright, narrow emission cores. To calculate the equivalent width of the H and K emission, we measured the excess emission in the line cores, normalizing by the integrated continuum intensity in a 1 \AA box far from line center.

In Figure 3 we plot the equivalent width of the Ca II H (dots) and K (asterisks) emission cores. While the equivalent widths are highly variable on short time scales, HD 35850 was only visible for a few hours each night. The limited sampling makes it difficult to estimate P_{rot} with these data alone. In Figure 4, we have phase-folded the summed H and K equivalent widths using $P_{\text{rot}} = 1.40 \text{ d}$ as derived from the DS photometry.

2.3. *EUVE* SW and MW Spectrometer Data

For the SW, MW, and LW spectroscopic data, the photon event data were screened to eliminate times of high background using the IRAF EUV package. Specifically, data were excluded when the total detector count rate exceeded 40 counts s^{-1} . The SW, MW, and LW photon event lists were used to create wavelength-calibrated FITS images and the SW, MW, and LW images were then analyzed within IDL.

We note that during the HD 35850 observation, the SW microchannel-plate detector developed a hot spot 8–12 detector pixels from the dispersion axis, close to the location of the Fe XXII 114 \AA line. A light curve of the hot spot intensity was used to identify the times when the hot spot flickered; those times were removed from the photon event list. Some hot pixels were still visible in the SW image, so a 9×9 pixel box around the hot spot was set to the local background level.

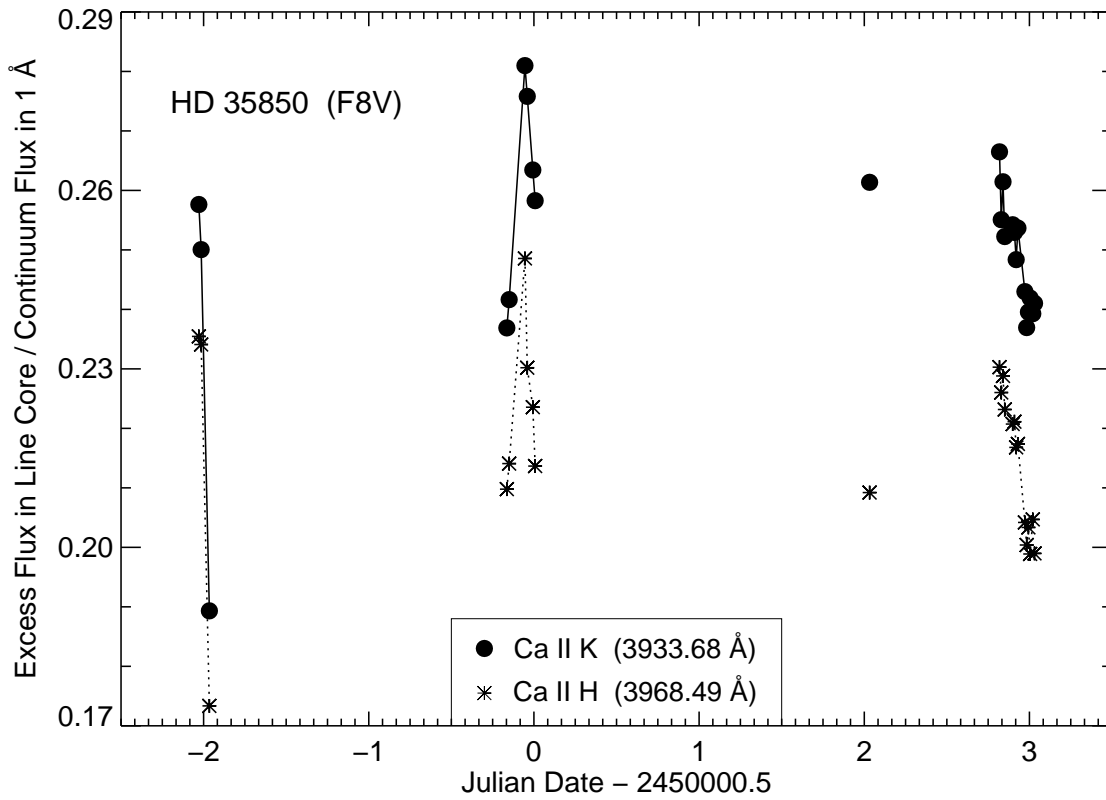


Fig. 3.— McMath-Pierce Solar-Stellar Spectrograph Ca II HK light curves of HD 35850 obtained 1995 October 2–12. For each exposure, we determined the excess emission in the line core in 1 \AA divided by the continuum flux in 1 \AA (i.e., the equivalent emission width).

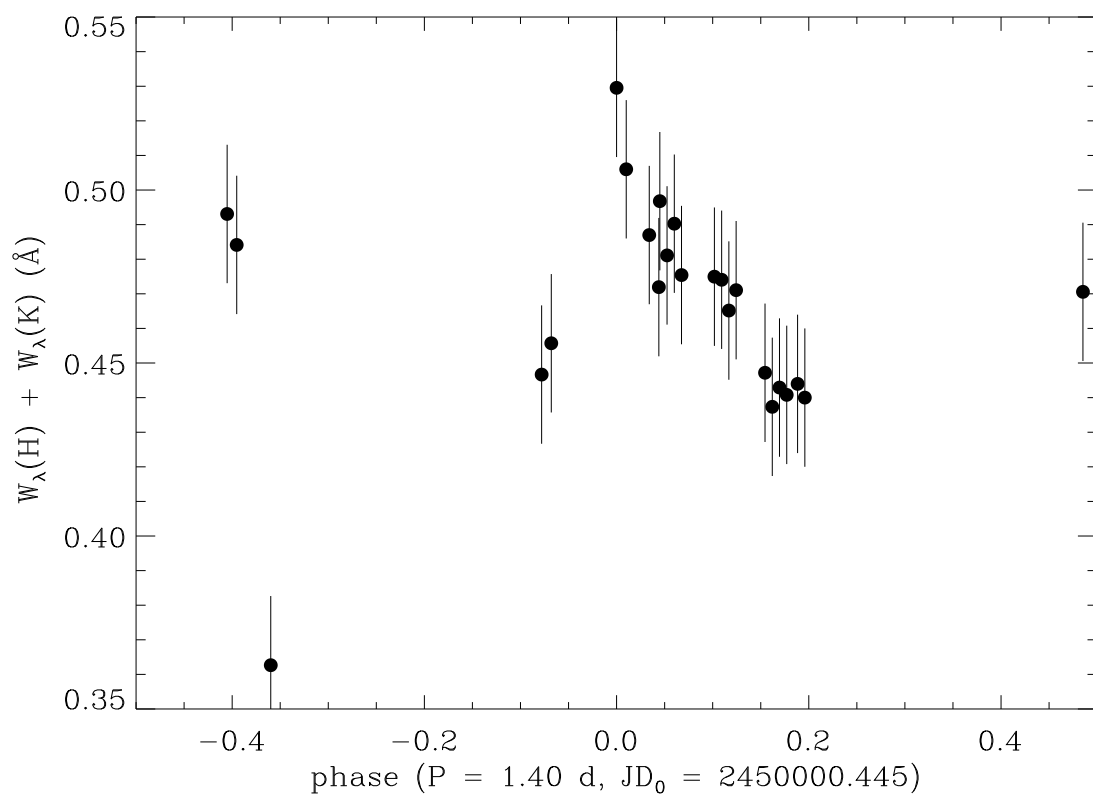


Fig. 4.— Phase-folded light curve of the combined Ca II H and K equivalent widths for a period of 1.405 d and zero-point of $\text{JD} = 2450000.445$, the time of Ca II HK emission maximum.

Spectra have been extracted from the SW, MW, and LW images using a modified version of the *IUE* SIPS spectral extraction algorithm (Lenz & Ayres 1992). The optimal extraction routine is specifically tailored to low S/N spectra from photon-counting devices like the *EUVE* and *IUE* spectrometers. Briefly, a raw SW, MW, or LW 2048×2048 pixel image is trimmed and compressed to 1024×290 and 2-pixel Gaussian smoothed. Since the spectra are over-sampled (no less than 7 detector pixels per resolution element), 2-pixel compression and smoothing improves S/N per bin without compromising spectral resolution. Using a predefined background region away from the source spectrum chosen to reduce curved edge effects caused by the *EUVE* reflection gratings, a background image is generated. A background-subtracted source image and corresponding error image are then created. The source image is used to measure the cross-dispersion profile. To perform an optimal extraction, each row in the source image is weighted by the cross-dispersion profile and the source spectrum and corresponding error are extracted using a 7-pixel aperture.

No emission lines longward of 365 \AA were detected in the LW count spectrum, presumably because of increased interstellar absorption at long wavelengths. Since the lines shortward of 365 \AA are measured in the MW spectrum, we did not consider the LW spectrum in our analysis. In Figures 5 and 6 (bottom panels), we show the flux-calibrated SW and MW spectra.

2.3.1. IDL Line and Continuum Fitting

In order to measure line fluxes, we have constructed a line list using the emissivity lists of Brickhouse et al. (1995), Monsignori Fossi & Landini (1993), and Mewe et al. (1985), in order of priority. Lines were grouped to match the SW and MW spectral resolution (0.5 and 1 \AA , respectively), allowing us to account for emissivity from blended lines. Based on the ionization states of the brightest identified lines, e.g., Fe XV, Fe XVI, and Fe XX, we made a starting guess at the plasma temperature ($\log T \approx 6.8$) and assumed a density $n_e = 10^{11} \text{ cm}^{-3}$. The line emissivities, spectrometer effective area curves, and exposure time were used to provide a starting guess for each line strength. The observed spectrum was then fit with multiple Gaussians, varying wavelength (\pm one resolution element) and line strength. Lines with fewer than 2σ counts were eliminated from the fit and the procedure was repeated. This way, line counts and upper limits were determined for all high-emissivity Fe IX to Fe XXIV lines.

The SW spectrum shows a small but detectable thermal bremsstrahlung continuum. To determine the SW continuum luminosity from $85\text{--}135 \text{ \AA}$, the continuum bins were fit with two parameters (emission measure and temperature) using the continuum emissivity model of Mewe et al. (1985). The Hipparcos distance to HD 35850 is 26.8 pc (Perryman et al. 1997). For HD 35850, the $85\text{--}135 \text{ \AA}$ continuum luminosity is $L_{\text{cont}} \approx 4.6 \pm 0.4 \times 10^{28} \text{ ergs s}^{-1}$.

In Figs. 5 and 6 (top and middle panels), we show the observed and fit count spectra with line identifications. Detected lines are indicated with dotted lines and upper limits are indicated with dashed lines. In Tables 1 and 2, we list the ion, possible blends, temperature of peak

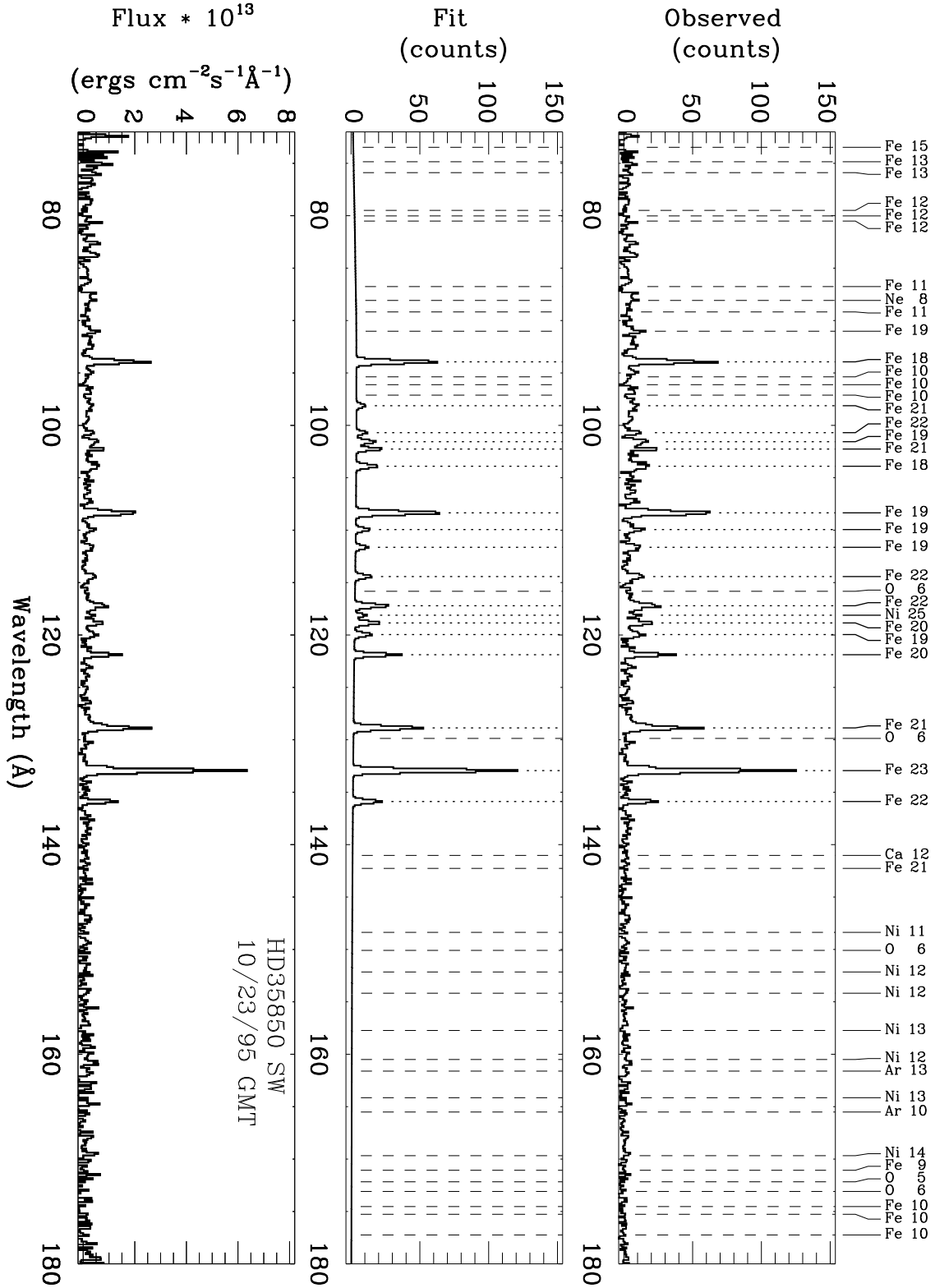


Fig. 5.— EUVE SW spectrum of HD 35850. *Top panel:* observed count spectrum (0.135 Å bins). *Middle panel:* detected (dotted lines) and undetected (dashed lines) SW lines plus continuum.

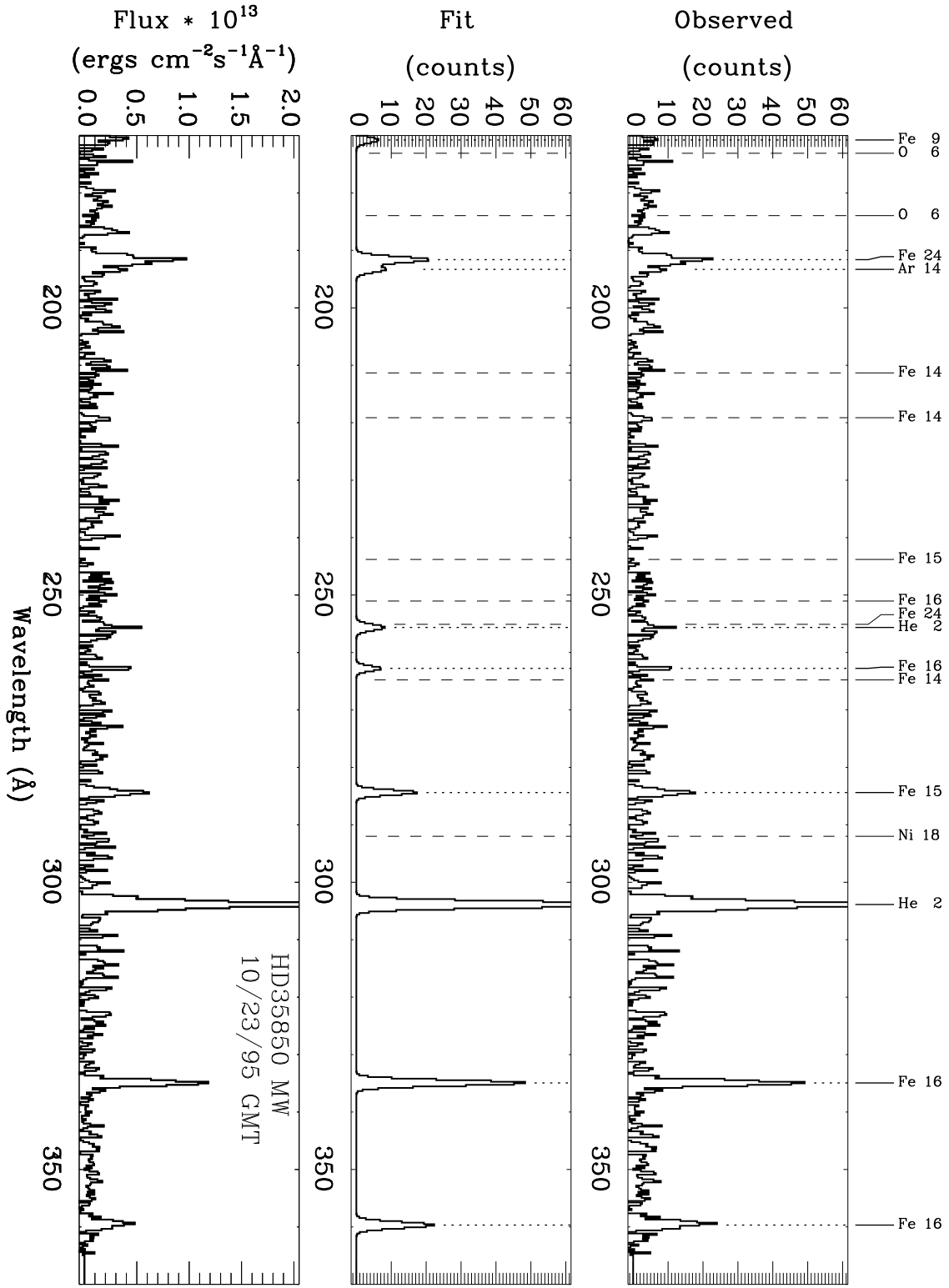


Fig. 6.— EUVE MW spectrum of HD 35850. *Top panel:* observed count spectrum (0.270 Å bins). *Middle panel:* detected (dotted lines) and undetected (dashed lines) MW lines. *Bottom panel:* flux-calibrated MW spectrum.

emissivity, laboratory and measured wavelengths, a detection flag, measured line luminosities, and the signal-to-noise ratio for detected lines. The line luminosities in Tables 1 and 2 use $N_{\text{H}} = 1.7 \times 10^{18} \text{ cm}^{-2}$ (see §2.3.3). In all, 28 distinct lines are detected above 2σ in the SW and MW spectra.

2.3.2. Electron-Density and Column-Density Estimates

The Fe XV and Fe XVI $\lambda\lambda 285, 335, 365$ line ratios are relatively insensitive to density and provide the best estimate of interstellar N_{H} in the *EUVE* bandpass. We find $N_{\text{H}} = 1.9 \pm 0.4 \times 10^{18} \text{ cm}^{-2}$.

Two density-sensitive line ratios can be measured accurately from the SW spectrum of HD 35850: Fe XXII $\lambda\lambda 114, 117$ and Fe XXI $\lambda\lambda 102, 129$. In Figure 7 we plot the observed SW spectrum (histogram) and fitted lines and continuum (solid line). The density-sensitive lines are indicated with dashed lines. The line Fe XXI line ratio is 0.22 ± 0.05 . The predicted branching ratio (solid curve) and observed line ratio (cross with 1σ error bar) are plotted versus density in Figure 8. Fig. 8 suggests that $\log n_e < 11.6 \text{ cm}^{-3}$. Consequently, we have chosen $\log n_e = 11.0 \text{ cm}^{-3}$ for the IDL and SPEX emission-measure analyses.

The Fe XXII line ratio is 0.47 ± 0.14 , suggesting $n_e > 10^{13} \text{ cm}^{-3}$. This ratio is unusually high and the implied density does not agree with the more reliable Fe XXI measurement. The detector hot spot (§ 2.3) may have contributed to the anomalous 114 Å flux. We note that line ratio calculations may have systematic uncertainties of up to 50% (Brickhouse et al. 1995) and that the derived density limit is only approximate.

2.3.3. IDL Emission-Measure Analysis

The measured line luminosities and upper limits have been used to estimate the coronal emission-measure distribution, $\text{Em}(T)$. Previous analyses of *EUVE* spectra (e.g., Güdel et al. 1997; Mewe et al. 1996) have generally relied on global fits to estimate $\text{Em}(T)$. For low S/N spectra like these, we prefer to use the bright lines in Tables 1 and 2 because (i) the emissivities of brighter lines have been fairly well established and (ii) the χ^2 statistic is not dominated by continuum bins.

We have excluded the He II $\lambda 304$ line from our analysis. On the Sun, the He II Ly α line is not a reliable temperature indicator: some, perhaps most, of the He II emission occurs in the chromosphere as a result of back-heating from the corona. We note also that around $\lambda 255$, the Fe XXIV line is blended with He II. The combined flux from both lines is listed as an upper limit in Table 2. For the remaining lines, our fitting procedure minimizes χ^2 between the measured and predicted line luminosities by varying the amplitude and shape of $\text{Em}(\log T)$ (in $\Delta \log T = 0.1$

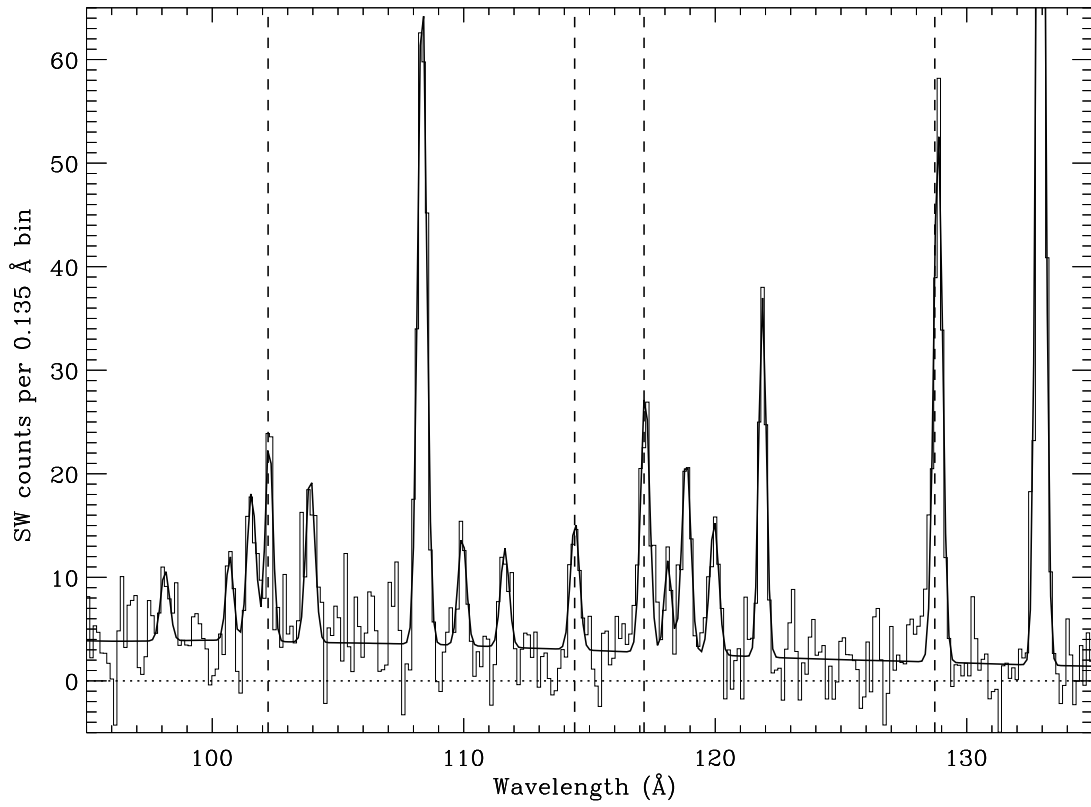


Fig. 7.— SW spectrum of HD 35850 in the 95–135 Å region (histogram) and our fit to the lines and continuum (solid curve). The dashed lines indicate the wavelength of the density-sensitive Fe XXI and Fe XXII lines.

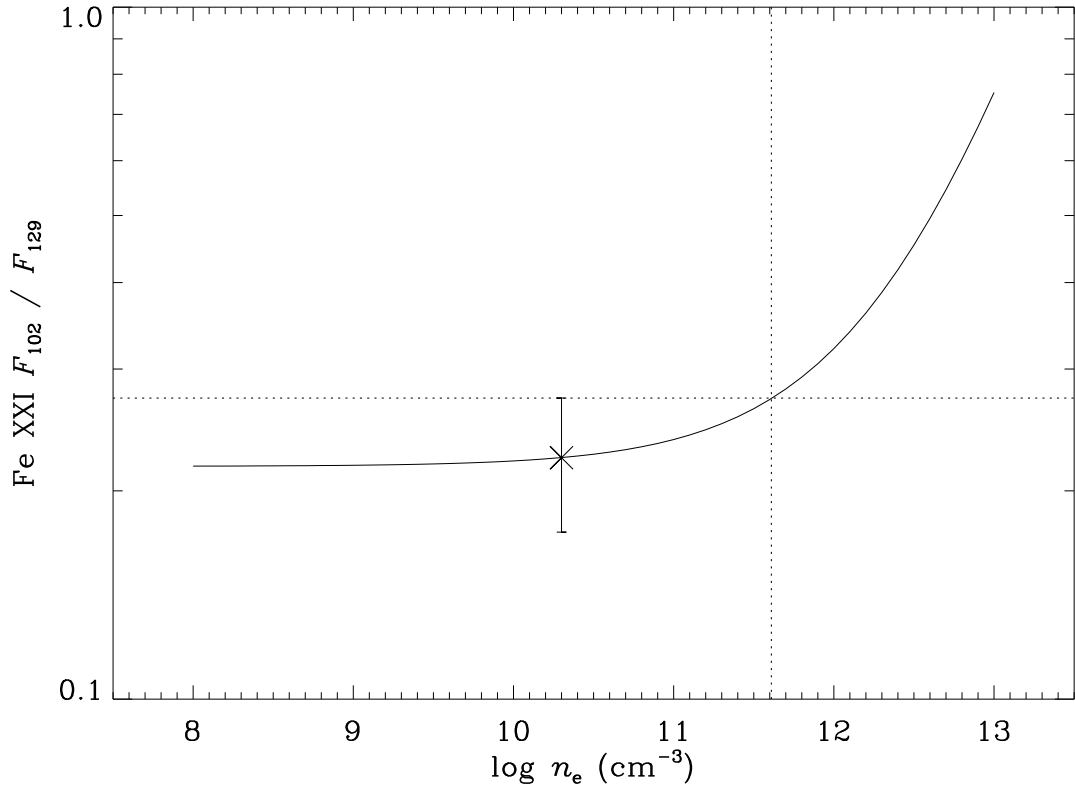


Fig. 8.— Fe XXI branching ratio as a function of $\log n_e$. The measured Fe XXI $\lambda\lambda 102, 129$ ratio and 1σ error are plotted. Based on the predicted branching ratio, we derive an upper limit $\log n_e < 11.6 \text{ cm}^{-3}$.

bins).

We use exponential Chebyshev polynomials (Lemen et al. 1989) to describe $\text{Em}(\log T)$. In addition to detected emission lines, the undetected Fe X to Fe XIV lines have been used as additional constraints in the non-linear least-squares fitting. The SW continuum luminosity serves to constrain Fe abundance.

Best-fit emission-measure distributions have been derived for a grid of column densities, Fe abundances, and Chebyshev-polynomial orders: $0.0 \leq N_{\text{H}} \leq 4.0 \times 10^{18} \text{ cm}^{-2}$, $0.1 \leq Z \leq 2.0$, and $2 \leq n \leq 11$, where Z is the coronal Fe abundance relative to the solar photospheric value of Anders & Grevesse (1989). We obtain acceptable χ_{ν}^2 values for all $n \geq 6$ and the resulting $\text{Em}(T)$ are characterized by peaks at $\log T \approx 6.8$ and $\log T \approx 7.4$. The best-fit column densities, abundances, and emission-measure distributions are not a strong function of n . As a result, we choose $n = 6$, the lowest polynomial order for which we obtain good fits.

Fits using different order polynomials orders, column densities, and abundances yield qualitatively similar results: prominent peaks in the emission-measure distribution at $\log T \approx 6.8$ and $\log T \approx 7.4$, although the sharpness of the high-T peak is not well constrained. The relative strength of the high-T component increases with increasing abundance. The best-fit emission-measure distributions all go to zero at very high temperatures ($\log T > 7.7$).

In Figure 9, we plot $\log \Delta\chi^2$ as a function of N_{H} and Z . The best fit ($\chi_{\nu}^2 \approx 1.07$) is obtained for $N_{\text{H}} = 1.7 \times 10^{18} \text{ cm}^{-2}$ and $Z = 1.15$. The 68% and 90% confidence contours are plotted for 9 free parameters (Z , N_{H} , and $n = 0, \dots, 6$). The *EUVE* line-to-continuum ratio yields $Z = 1.15^{+0.75}_{-0.35}$. To obtain substantially sub-solar abundances ($Z < 0.5$), would require more than doubling the continuum level (dark solid line in Fig. 7). This is not compatible with the background-subtracted SW spectrum. We have experimented with various background-subtraction algorithms (smoothed, unsmoothed, polynomial fit): all produce bright lines and a weak continuum.

We find adequate fits for a range of column densities and abundances, and, in particular, we find $\chi_{\nu}^2 \approx 1.15$ for $N_{\text{H}} = 1.4 \times 10^{18} \text{ cm}^{-2}$ and $Z = 1$. We adopt these values in Figs. 10–14. In Figure 10, the observed and predicted line luminosities for detected (filled circles) and undetected (open triangles) lines are compared, with a factor of two deviation indicated with dashed lines. Note the anomalously high Fe XXII line flux (see §2.3.2). In Figure 11, we plot $\text{Em}(\log T)$ per $\log T$ bin of 0.1 dex as derived from the IDL line analysis (dash-dotted line).

2.3.4. *SPEX Differential Emission-Measure Analysis*

In order to verify the results of the IDL line analysis, we performed a differential emission measure analysis of the optimally-extracted *EUVE* SW and MW spectra using the SPEX code (see Kaastra et al. 1992 for a detailed description of the DEM method and the SPEX Collisional Ionization Equilibrium model). For fixed values of N_{H} and Z , we derived $\text{Em}(T)$ using the SPEX

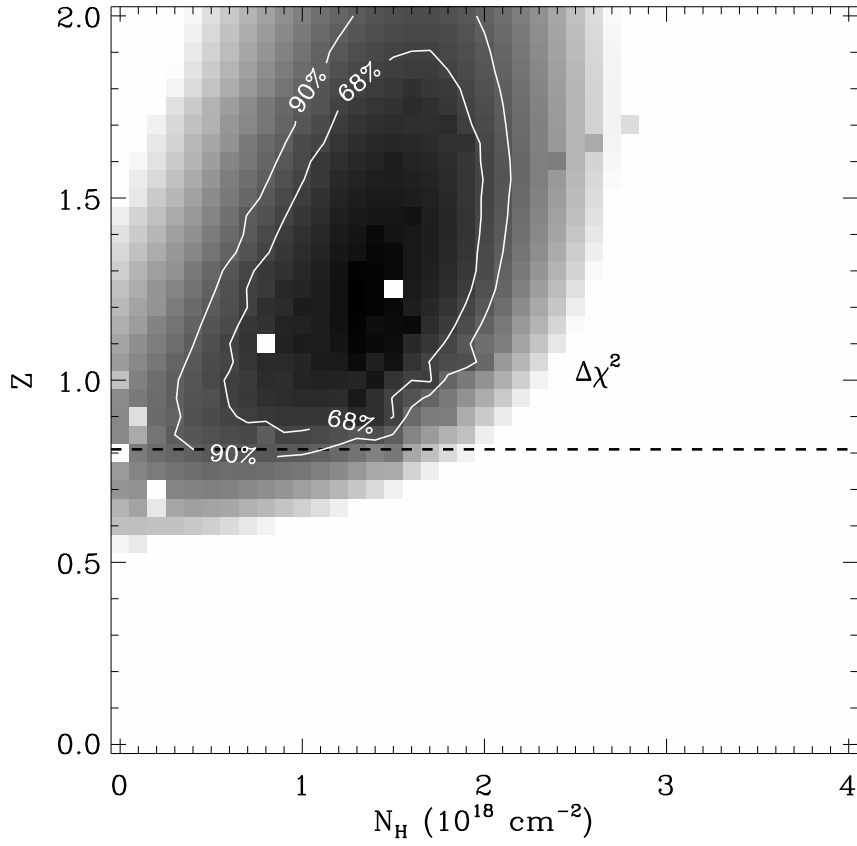


Fig. 9.— Grid of $\log \Delta\chi^2$. The SW and MW lines and continuum luminosities were fit using 8th-order Chebyshev polynomials to describe $\text{Em}(\log T)$ at each point in the Z versus N_{H} plane, where Z is the coronal Fe abundance relative to the solar photospheric values of Anders & Grevesse (1989). Dark pixels indicate regions of low χ^2 . The 68 and 90% confidence contours for 9 free parameters are shown.

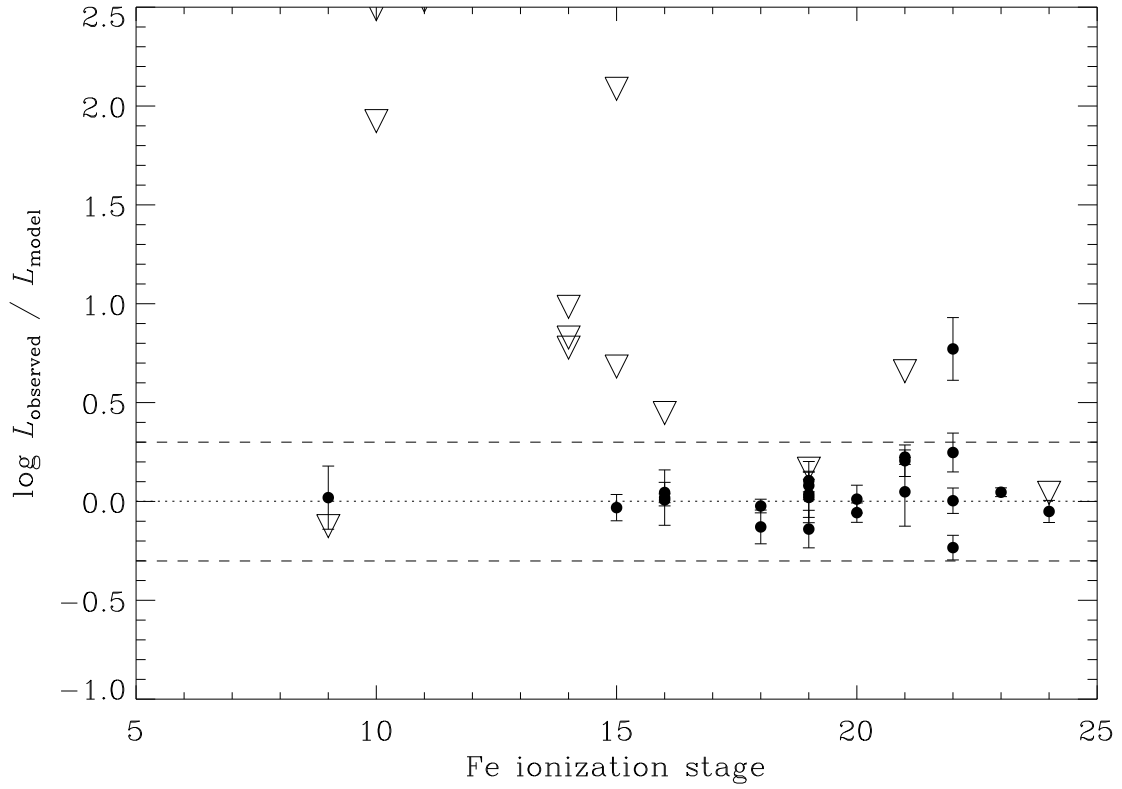


Fig. 10.— Comparison of observed to predicted line luminosities for a range of Fe ionization states for $Z = 1$, $N_{\text{H}} = 1.4 \times 10^{18} \text{ cm}^{-2}$, and $\log n_e = 11.0 \text{ cm}^{-3}$. Downward-pointing triangles indicate upper limits for high-emissivity, undetected lines. Note the discrepant Fe XXII measurement.

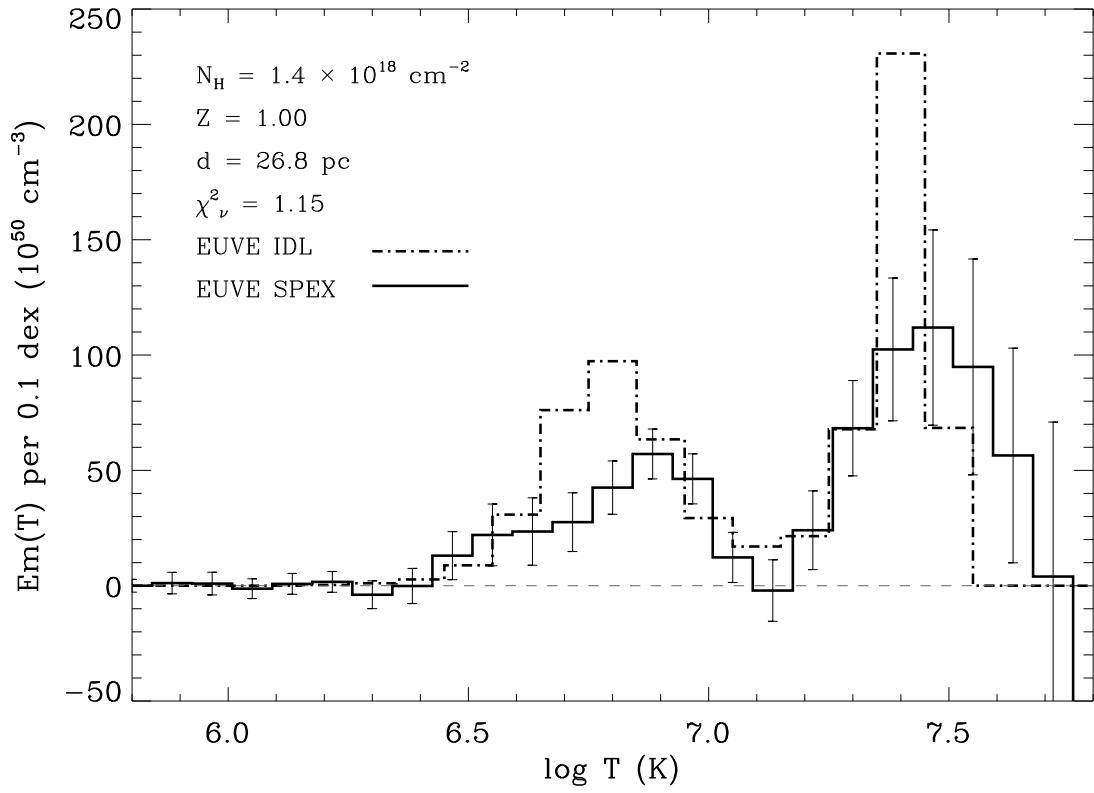


Fig. 11.— Best-fit emission-measure distribution based on the IDL (dash-dotted line) and SPEX (solid line and error bars) analyses of the EUVE SW and MW lines and continuum.

regularization method. In Fig. 11, we plot $\text{Em}(T)$ for $N_{\text{H}} = 1.4 \times 10^{18} \text{ cm}^{-2}$ and $Z = 1$ (solid line). The IDL and SPEX analyses yield similar emission-measure distributions, with 55–60% of the emission measure in the hotter component above $\log T = 7$.

2.4. ASCA SIS data

An 18-ks *ASCA* exposure of HD 35850 obtained in 1995 has been analyzed by Tagliaferri et al. (1997). We use their reduced *ASCA* SIS0 spectrum to further constrain the *EUVE* results. Because the SIS cannot resolve individual emission lines from coronal sources, we cannot use the IDL line analysis method described in § 2.1.4. Consequently, we fitted the *ASCA* SIS0 spectrum using the SPEX DEM code. For the SIS0 fits, N_{H} was fixed at $1.4 \times 10^{18} \text{ cm}^{-2}$. The best-fit abundance using the DEM collisional ionization equilibrium (CIE) model is $Z \approx 0.5$ with acceptable fits in the range 0.34–0.81. The *ASCA* upper bound on Z is plotted in Fig. 9 as a dashed line. We note that $Z \approx 0.8$ is marginally compatible with *EUVE* and *ASCA*.

To illustrate, the *ASCA* SIS0 data are shown in Figure 12 (points) with the DEM model spectrum (histogram) for $Z = 1$. Discrepancies between the SIS data and the $Z = 1$ model are seen around 1.2 keV and 2.4 keV. These are the spectral features which normally drive the fit towards lower abundances. Brickhouse et al. (1997) have identified a complex of lines from 1.0–1.3 keV from highly excited ($n > 5$), highly ionized (Fe XVII to Fe XXV) states that are missing from the plasma codes in XSPEC and SPEX. The missing lines may partly explain the large discrepancy around 1.2 keV.

In Figure 13, we show the corresponding *ASCA* SPEX $\text{Em}(\log T)$ for $Z = 1$. Like the *EUVE* emission-measure distributions, the *ASCA* $\text{Em}(T)$ peaks at $\log T$ of 6.7 and 7.4. Finally, we note that the *EUVE* count rates are higher than expected from the SIS spectrum. Based on the SIS emission-measure analysis, the expected *EUVE* DS count rate is approximately $0.16 \text{ counts s}^{-1}$, indicated in Fig. 1 as a dashed line. HD 35850 appears to have been more active (by $\sim 25\%$) during the *EUVE* observation.

2.5. Comparison with Previous Results

For HD 35850, we find that the *EUVE* line-to-continuum ratio indicates approximately solar coronal Fe abundance while a SPEX DEM analysis of the *ASCA* SIS0 spectrum is consistent with moderately sub-solar abundances. We note that HD 35850’s photospheric Fe abundance is close to solar (Tagliaferri et al. 1994). Analyses of other active coronal sources often find coronal abundances far below the measured photospheric abundances (e.g., AB Dor, Mewe et al. 1996).

The *ASCA* SIS and GIS spectra of HD 35850 were fit by Tagliaferri et al. (1997) using a number of multi-temperature plasma models in XSPEC (Arnaud 1996). For example, the best-fit

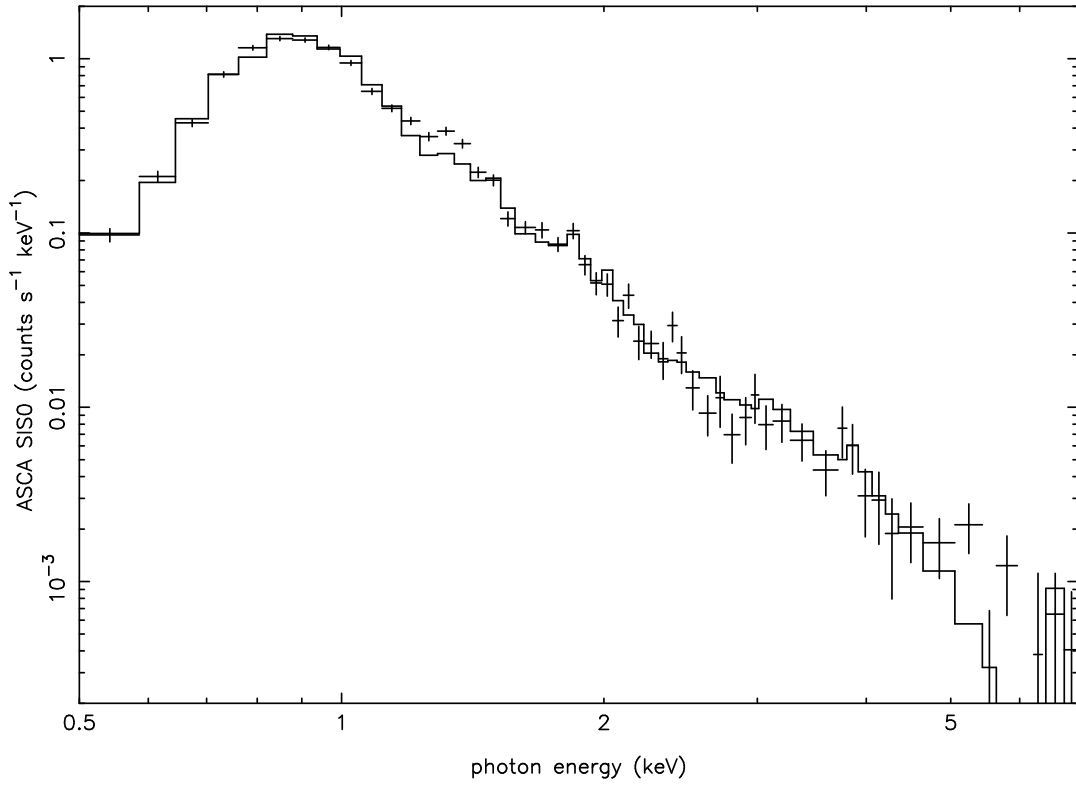


Fig. 12.— The 18 ks ASCA SIS0 spectrum of HD 35850 obtained 1995 March 12 (points and error bars). The best-fit SPEX DEM model (not shown) indicates sub-solar Fe abundances, $0.34 < Z < 0.81$. The model shown (solid histogram) assumes $Z = 1$, $N_{\text{H}} = 1.4 \times 10^{18} \text{ cm}^{-2}$, and $\log n_e = 11.0 \text{ cm}^{-3}$. The SIS0 spectrum is generally consistent with solar abundances aside from serious departures around 1.2 keV and 2.4 keV.

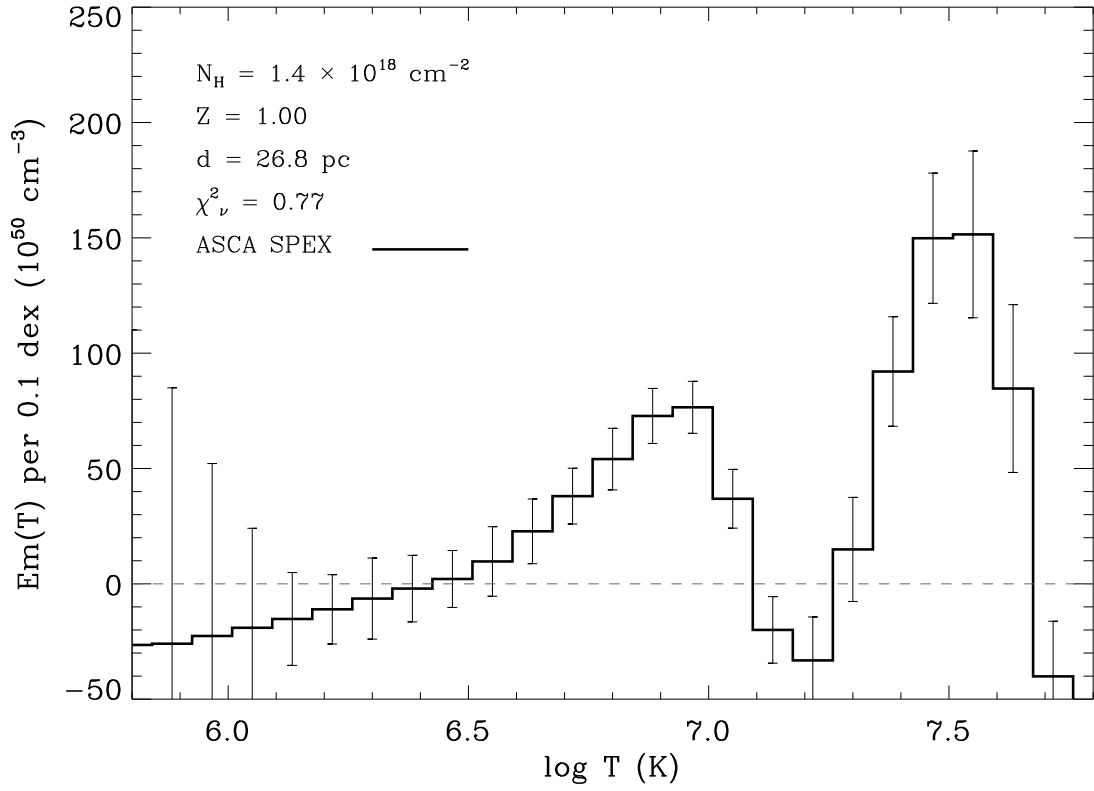


Fig. 13.— Emission-measure distribution based on the SPEX global-fitting of the ASCA SIS0 spectrum. The EUVE and ASCA data were not obtained simultaneously. Poor fits resulted when both data sets were modeled together.

SIS0 MEKAL parameters indicate a two-temperature corona ($kT_1 \approx 0.6$ keV and $kT_2 \approx 1.2$ keV) with sub-solar abundances ($0.12 < Z < 0.25$). Tagliaferri et al. (1997) also performed a combined PSPC/SIS/GIS analysis using a 5-ks *ROSAT* PSPC observation of a field near HD 35850. The combined analysis involved comparing 2-T and 3-T MEKAL and RS models in XSPEC with solar and non-solar abundances and using different cross-detector normalization constraints (see their Table 5 and Figure 3). The XSPEC fits generally favor sub-solar abundance models; the best-fit MEKAL 3-T model yields $Z = 0.34 \pm 0.04$, $T_1 = 0.52 \pm 0.07$, $T_2 = 0.78_{-0.09}^{+0.15}$, and $T_3 = 1.9_{-0.4}^{+1.0}$, with $\approx 47\%$ of the total emission measure in the coolest component. This cool component is the $\log T = 6.8$ component seen in the *EUVE* DEM. The two hottest components appear to represent the hotter DEM component. Our DEM analysis of the *ASCA* SIS spectra yields somewhat higher abundances ($0.34 < Z < 0.81$) than Tagliaferri et al. (1997) and somewhat lower Fe abundance than our *EUVE* analysis.

Systematic differences between *ASCA* and *EUVE* analyses have been reported for other bright coronal sources. For example, Brickhouse et al. (1997) obtained simultaneous observations of Capella with *ASCA* and *EUVE* in 1996 March. As with previously obtained *EUVE* spectra of Capella, they find essentially solar photospheric Fe abundance. On the other hand, the plasma codes in XSPEC yield consistently poorer fits to the *ASCA* SIS spectra of Capella and require sub-solar abundances ($Z \approx 0.7$).

Note: After the submission of this paper, a preprint of a paper to appear in *Astronomy and Astrophysics* by Mathioudakis & Mullan (1998) came to our attention which analyzes the *EUVE* observations of HR 1817=HD 35850. This paper and the Mathioudakis & Mullan paper arrive at substantially different conclusions regarding the Fe abundance of HD 35850. Mathioudakis & Mullan (1998) visually compare the observed *EUVE* SW and MW spectra with synthetic spectra based on the 3-T MEKAL model suggested by Tagliaferri et al. (1997). They conclude that the *EUVE* spectra are consistent with Tagliaferri et al. (1997) and are inconsistent with any solar-abundance model, particularly because the Fe XIII–Fe XV lines in the MW spectrum are so weak. While it is difficult to visually compare spectra, their observed and synthetic MW spectra appear to be quite different: the predicted lines are weak and the the low- Z model appears to over-predict the MW continuum (see Figures 2 and 5 in Mathioudakis & Mullan 1998). Given the limitations of *ASCA* and *EUVE*, higher-resolution, higher-S/N *AXAF* HETG or *XMM* RGS spectra may be needed to determine HD 35850’s coronal abundance.

3. Microflaring

The double-peaked EM distribution observed on three active, solar-type stars has been modeled by Güdel (1997) on the basis of a simplified stochastic flare model derived from the solar nanoflare model of Kopp & Poletto (1993). Rather than approaching the EM distribution problem hydrostatically, as is the case when using loop scaling laws, Kopp & Poletto (1993) use a simplified hydrodynamic model to treat a large number of flares.

The flare model reduces the loop hydrodynamics to a point model with a chromospheric energy sink. A series of energy pulses of finite duration is fed into the loop. This heating energy is lost by conduction into the chromosphere and by radiation into space. Without flaring, all loops are kept at the same equilibrium temperature dictated by hydrostatic loop scaling laws (Rosner, Tucker, & Vaiana 1978). Therefore, our model starts out at a lower threshold temperature and does not consider cooler loops. The salient feature of this model is its phenomenological similarity with more sophisticated hydrodynamic simulations in terms of the emission measure, temperature, and radiation history. The point model cannot treat the more complicated 1-D problem of radiation and conduction occurring between the corona, the transition region, and the chromosphere. The need to simulate a large number of flares requires such a simplified approach.

Flares are ignited in each loop randomly distributed in time but satisfying a statistical number distribution in total flare energy E above a pre-defined threshold energy. I.e., $dN/dE \propto E^{-\alpha}$ where $N(E)$ is the number density of flares in the energy interval $[E, E + dE]$. On the basis of solar and stellar optical flare monitoring, $1.8 < \alpha < 2.0$ has been suggested by Hudson (1991). For consistency with Güdel (1997), we chose a threshold energy $E > 10^{27}$ ergs. In order to reduce the number of free parameters, all loops have the same height and vary only in their thickness between a minimum of 6.4×10^6 cm and a maximum of 4.3×10^9 cm to accommodate the range of flare energies. Each run produces a large number of small flares and only a small number of very large flares. Because no very large flares were observed by *EUVE*, the largest flares in the simulations were eliminated.

The total EM distribution is determined by averaging (in time and space) the EM distribution of all loops. Similarly, the light curve is the superposition of coronal radiation leaving the star into 2π steradians, i.e., half the radiative losses are absorbed in the chromosphere, half are radiated into space. We have experimented with various parameters and find that our model reproduces the required coronal luminosity and EM distribution only if we assume compact loops, with a semi-length of 2.6×10^9 cm and essentially full surface coverage. The simulations provide fairly tight constraints on the power-law index of flare energies ($\alpha \approx 1.8$). In this case, the equilibrium temperature is 6×10^6 K.

Our best-fit microflare model for HD 35850 uses 1100 loops, distributed evenly over the star's surface, and accommodating 2.64×10^7 flares during a typical observation lasting 5×10^5 s. The resulting EM distribution is shown in Figure 14. The soft X-ray light curves from these simulations show the same 1–12 hour variability seen in *ASCA* SIS and *EUVE* DS light curves. Because the power-law distribution of flares favors small (microflare) events, the simulated light curves also show lower-amplitude, shorter-time scale variability seen in higher-S/N X-ray observations of dMe stars but not discernible for HD 35850.

The model EM distribution exhibits the characteristic two-temperature structure with a broad intermediate minimum. However, in this model the EM structure is not just a result of radiative cooling as suggested by Gehrels & Williams (1993). It is a consequence of the balance

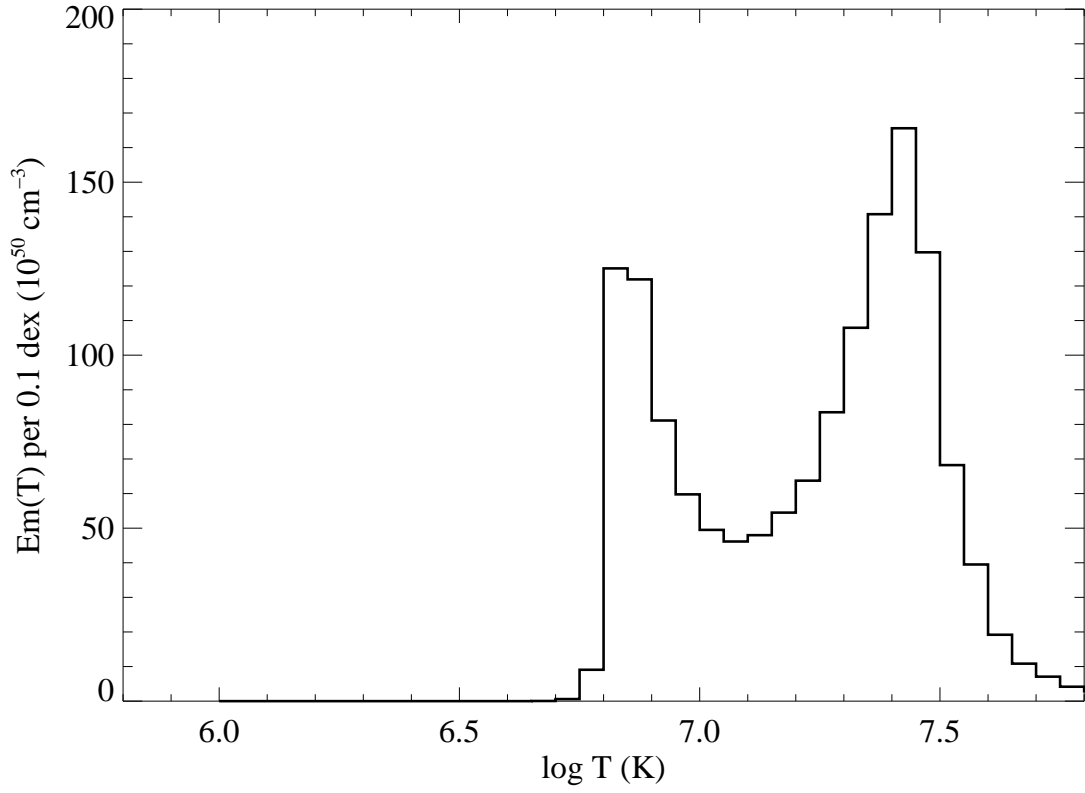


Fig. 14.— Emission-measure distribution produced by the microflaring model if we assume $\alpha = 1.8$, compact loops, with a semi-length of 2.6×10^9 cm, and full surface coverage. In this case, the equilibrium temperature is $T \approx 6 \times 10^6$ K and a dominant peak occurs near $T \approx 26 \times 10^6$ K.

between flare heating, cooling by conduction, and cooling by radiation. Given our simplistic model, it is noteworthy that the two-temperature structure (or rather the broad minimum around 10 MK) observed on many active normal stars can be explained, in part, by a hydrodynamic property of frequently-flaring loops.

4. The Active Corona of HD 35850

We summarize the combined *EUVE* and *ASCA* results for HD 35850 in Table 3. The *ASCA* SIS spectral analysis suggests sub-solar abundances and the *EUVE* line-to-continuum ratio indicates approximately solar photospheric abundances. Although $Z \approx 0.8$ is marginally consistent with the *EUVE* and *ASCA* spectra, all the *ASCA* analyses yield systematically lower Fe abundance than the *EUVE* Fe line-to-continuum ratio.

Assuming photospheric abundances, the corona is characterized by emission measure in a warm component from 5–8 MK and a hot component from 21–30 MK. Like other rapidly rotating, Pleiades-age dwarfs, HD 35850 appears to represent an activity extremum for main-sequence solar-type stars. HD 35850’s inverse Rossby number is $\tau_c/P_{\text{rot}} \approx 20.7/1.40 \approx 15$ and its X-ray surface flux is $F_X \approx 1.8 \times 10^7 \text{ ergs s}^{-1} \text{ cm}^{-2}$. For AB Dor (K0 V), $F_X \approx 1.7 \times 10^7 \text{ ergs s}^{-1} \text{ cm}^{-2}$ (Hempelmann et al. 1995) and $\tau_c/P_{\text{rot}} > 120$. For EK Dra (G0 V), $F_X \approx 1.5 \times 10^7 \text{ ergs s}^{-1} \text{ cm}^{-2}$ and $\tau_c/P_{\text{rot}} \approx 15$. AB Dor, HD 35850, and EK Dra appear to have saturated or nearly saturated X-ray activity and, despite having more rapid rotation and a deeper convection zone, AB Dor’s X-ray surface flux is the same as HD 35850’s.

The *EUVE* DS light curve of HD 35850 shows about one moderate-amplitude (40% increase) flare per day. The X-ray and EUV variability and the presence of substantial emission measure above 20 MK suggests that some flare-like mechanism must be heating the corona. To test this hypothesis, we have modeled HD 35850’s light curves and $\text{Em}(T)$ using the hydrodynamic microflare point model of Güdel (1997). The simulations suggest a power-law index of flare energies $\alpha \approx 1.8$.

On the Sun, transient brightenings seen in *Yohkoh* Soft X-ray Telescope images of solar active regions provide a direct measure of the microflaring amplitude and power-law index. Microflaring can provide, at most, 20% of the heating rate required to power the active-region corona (Shimizu 1995). Ofman, Davila, & Shimizu (1996) have shown that the transient brightenings seen by *Yohkoh* may be a consequence of resonant absorption of global-mode Alfvén waves in coronal loops, excited by random footpoint motions of these loops. A more recent analysis of *Yohkoh* data suggests that a steeper distribution of smaller flares, the so-called nanoflares, may also be present (Shimizu & Tsuneta 1997). Whether the microflares occur as a result of Alfvén waves or magnetic reconnection, they cannot account for the radiative output of the Solar corona. For the rapidly rotating F and G dwarfs, however, the microflare models are able to reproduce the observed luminosity, EM distribution, and variability.

To better test microflaring on stars, accurate coronal density and abundance measurements as a function of temperature are needed to better constrain the emission-measure distribution. Photospheric magnetic field strength and filling fractions can further constrain loop models. Also, higher S/N, higher cadence hard and soft X-ray light curves will provide a statistically robust estimate of the distribution of flares. Planned observations of AB Dor with the *Advanced X-ray Astrophysics Facility's* High-Energy Transmission Grating Spectrometer will help resolve some of the density and abundance issues discussed in this paper and may lead to more quantitative tests of coronal heating models.

MG would like to thank Tom Ayres for providing some of the IDL routines to perform optimal extraction and line fitting. MG made extensive use of the NASA Astrophysics Data System abstract service, the HEASARC database at NASA/GSFC, and the Simbad database at the Centre de Données astronomiques de Strasbourg. The authors would like to thank an anonymous referee for many helpful suggestions. This research was supported under NASA grant NAG-2891 to the University of Colorado.

REFERENCES

- Anders, E. & Grevesse, N. 1989, *Geochimica et Cosmochimica Acta*, 53, 197
- Arnaud, K.A. 1996, *Astronomical Data Analysis Software and Systems V*, eds. G.H. Jacoby & J. Barnes, ASP Conference Series, 101, 17
- Baliunas, S.L., et al. 1995, *ApJ*, 438, 269
- Baliunas, S.L., Nesme-Ribes, E., Sokoloff, D., & Soon, W.H. 1996, 460, 848
- Benz, A.O., & Güdel, M. 1994, *A&A*, 285, 621
- Blackwell, D.E., & Lynas-Gray, A.E. 1994, *A&A*, 282, 899
- Brickhouse, N.S., Raymond, J.C., & Smith, B.W. 1995, *ApJS*, 97, 551
- Brickhouse, N.S., Dupree, A.K., Edgar, R.J., Drake, S.A., White, N.E., Liedahl, D.A., Singh, K.P. 1997, *AAS*, 191, 2513
- Cutispoto, G., Tagliaferri, G., Giommi, P., Gouiffes, C., Pallavicini, R., Pasquini, L., & Rodonó, M. 1991, *A&AS*, 87, 233
- Donati, J.-F., & Collier Cameron, A. 1997, *MNRAS*, 291, 1
- Feigelson, E.D., & Babu, G.J. 1992, *Statistical Challenges in Modern Astronomy*, (Springer-Verlag: New York)
- Field, G.B. 1965, *ApJ*, 142, 531
- Gehrels, N., & Williams, E.D. 1993, *ApJ*, 418, L25
- Gray, D.F., & Baliunas, S.L. 1997, *ApJ*, 475, 303

- Güdel, M. Guinan, E.F., Mewe, R., Kaastra, J., & Skinner, S.L. 1997, ApJ, 483, 947
- Güdel, M. 1997, ApJ, 480, L121
- Haisch, B., Bowyer, S., & Malina, R. 1993, JBIS, 46, 331
- Haisch, B., & Schmitt, J.H.M.M. 1996, PASP, 108, 113
- Halpern, J., & Marshall, H. 1996, ApJ, 464, 760
- Hempelmann, A., Schmitt, J.H.M.M., Schultz, M., Rüdiger, G., & Stępień, K. 1995, A&A, 294, 515
- Kaastra, J.S. 1992, *An X-ray spectral code for optically thin plasmas*, internal SRON-Leiden Report, updated version 2.0
- Kim, Y.-C., & Demarque, P. 1996, ApJ, 457, 340
- Kopp, R.A., & Polletto, G. 1993, ApJ, 418, 496
- Kürster, M., Schmitt, J.H.M.M., Cutispoto, G., & Dennerl, K. 1997, A&A, 320, 831
- Lemen, J.R., Mewe, R., Schrijver, C., & Fludra, A. 1989, ApJ, 341, 474
- Lenz, D.D., & Ayres, T.R. 1992, PASP, 104, 1104
- Mathioudakis, M., & Mullan, D.J. 1998, A&A, in press
- Mewe, R., Kaastra, J., White, S.M., Pallavicini, R. 1996, A&A, 315, 170
- Mewe, R., Lemen, J.R., Peres, G., Schrijver, C., Serio, S., A&A, 152, 229
- Monsignori Fossi, B., & Landini, M. 1994, Sol. Phys., 152, 81
- Noyes, R., Hartmann, L., Baliunas, S., Duncan, D., & Vaughn, A. 1984, ApJ, 279, 763
- Ofman, L., Davila, J.M., & Shimizu, T. 1996, ApJ, L39
- Oreshina, A.V. & Somov, B.V. 1997, A&A, 320, L53
- Parker, E.N. 1953, ApJ, 117, 431
- Perryman, M.A.C., et al. 1997, A&A, 323, L49
- Poletto, G., Pallavicini, R., & Kopp, R.A. 1988, A&A, 201, 93
- Rutten, R.G.M., Schrijver, C.J., Lemmens, A.F.P., & Zwaan, C. 1991, A&A, 252, 203
- Scargle, J.D. 1989, ApJ, 343, 874
- Shimizu, T. 1995, PASJ, 47, 251
- Shimizu, T., & Tsuneta, S. 1997, ApJ, 486, 1045 ApJ, 296, 46
- Tagliaferri, G., Cutispoto, G., Pallavicini, R., Randich, S., & Pasquini, L. 1994, A&A, 285, 272
- Tagliaferri, G., Covino, S., Fleming, T.A., Gagné, M., Pallavicini, R., Haardt, F., & Uchida, Y. 1997, A&A, 321, 850
- Wood, B.E., Harper, G.M., Linsky, J.L., & Dempsey, R.C. 1996, ApJ, 458, 761

Table 1. HD 35850: 1995 October 23–30: EUVE SW Lines

| Dominant Ion | Blended Ion | $\log T$ (K) | λ_{lab} (Å) | λ_{obs} (Å) | Detect Flag | L_{line} (10^{27} ergs s $^{-1}$) | S/N |
|--------------|-------------|--------------|----------------------------|----------------------------|-------------|--|-------|
| Fe XV | | 6.3 | 73.47 | ... | N | <6.00 | ... |
| Fe XIII | | 6.2 | 74.85 | ... | N | <4.43 | ... |
| Fe XIII | Fe XIII | 6.2 | 75.89 | ... | N | <4.47 | ... |
| Fe XII | | 6.2 | 79.49 | ... | N | <2.40 | ... |
| Fe XII | | 6.2 | 80.02 | ... | N | <2.13 | ... |
| Fe XII | | 6.2 | 80.51 | ... | N | <2.14 | ... |
| Fe XI | Fe XI | 6.1 | 86.76 | ... | N | <1.28 | ... |
| Ne VIII | | 5.8 | 88.08 | ... | N | <1.20 | ... |
| Fe XI | Fe XI | 6.1 | 89.18 | ... | N | <1.08 | ... |
| Fe XIX | | 6.9 | 91.02 | ... | N | <1.04 | ... |
| Fe XVIII | Fe XX | 6.8 | 93.92 | 93.94 | Y | 8.87 | 12.08 |
| Fe X | | 6.1 | 95.37 | ... | N | <0.90 | ... |
| Fe X | | 6.1 | 96.12 | ... | N | <0.91 | ... |
| Fe X | | 6.1 | 97.12 | ... | N | <0.91 | ... |
| Fe XXI | Ne VIII | 7.0 | 97.88 | 98.13 | Y | 0.98 | 2.03 |
| Fe XXII | | 7.1 | 100.78 | 100.70 | Y | 0.93 | 2.27 |
| Fe XIX | | 6.9 | 101.55 | 101.56 | Y | 1.96 | 4.09 |
| Fe XXI | | 7.0 | 102.22 | 102.26 | Y | 2.24 | 4.97 |
| Fe XVIII | | 6.8 | 103.94 | 103.90 | Y | 2.21 | 4.60 |
| Fe XIX | Fe XXI | 6.9 | 108.37 | 108.35 | Y | 8.49 | 13.17 |
| Fe XIX | | 6.9 | 109.97 | 109.94 | Y | 1.36 | 3.24 |
| Fe XIX | Ni XXIII | 6.9 | 111.70 | 111.63 | Y | 1.27 | 2.93 |
| Fe XXII | | 7.1 | 114.41 | 114.42 | Y | 1.79 | 3.94 |
| O VI | | 5.5 | 115.83 | ... | N | <0.83 | ... |
| Fe XXII | Fe XXI | 7.1 | 117.17 | 117.21 | Y | 3.83 | 6.48 |
| Ni XXV | | 7.2 | 117.95 | 118.12 | Y | 1.14 | 2.62 |
| Fe XX | | 7.0 | 118.66 | 118.85 | Y | 2.99 | 5.68 |
| Fe XIX | | 6.9 | 120.00 | 119.96 | Y | 2.07 | 4.01 |
| Fe XX | | 7.0 | 121.83 | 121.88 | Y | 4.87 | 8.37 |
| Fe XXI | | 7.0 | 128.73 | 128.86 | Y | 10.03 | 11.41 |
| O VI | | 5.5 | 129.87 | ... | N | <1.10 | ... |
| Fe XXIII | Fe XX | 7.1 | 132.85 | 132.94 | Y | 24.61 | 19.19 |
| Fe XXII | | 7.1 | 135.78 | 135.89 | Y | 4.93 | 6.27 |
| Ca XII | | 6.3 | 141.03 | ... | N | <1.52 | ... |
| Fe XXI | | 7.0 | 142.27 | ... | N | <1.63 | ... |

Table 1—Continued

| Dominant Ion | Blended Ion | $\log T$ (K) | λ_{lab} (Å) | λ_{obs} (Å) | Detect Flag | L_{line} (10^{27} ergs s $^{-1}$) | S/N |
|-----------------|----------------|-----------------|-------------------------------|-------------------------------|----------------|---|-----|
| Ni XI | | 6.2 | 148.37 | ... | N | <1.66 | ... |
| O VI | | 5.5 | 150.09 | ... | N | <1.82 | ... |
| Ni XII | | 6.2 | 152.15 | ... | N | <1.95 | ... |
| Ni XII | | 6.2 | 154.18 | ... | N | <2.06 | ... |
| Ni XIII | Ni X | 6.3 | 157.73 | ... | N | <2.22 | ... |
| Ni XII | Ni XIII | 6.3 | 160.50 | ... | N | <2.68 | ... |
| Ar XIII | Ca XIII | 6.4 | 161.61 | ... | N | <2.64 | ... |
| Ni XIII | Ar XIII | 6.3 | 164.15 | ... | N | <3.04 | ... |
| Ar X | | 6.1 | 165.51 | ... | N | <2.81 | ... |
| Ni XIV | | 6.3 | 169.68 | ... | N | <3.14 | ... |

Table 2. HD 35850: 1995 October 23–30: EUVE MW Lines

| Dominant Ion | Blended Ion | $\log T$ (K) | λ_{lab} (Å) | λ_{obs} (Å) | Detect Flag | L_{line} (10^{27} ergs s $^{-1}$) | S/N |
|--------------|-------------|--------------|----------------------------|----------------------------|-------------|--|-------|
| Fe IX | | 5.8 | 171.07 | 170.78 | Y | 4.78 | 2.25 |
| O VI | | 5.5 | 173.09 | ... | N | <3.45 | ... |
| O VI | | 5.5 | 183.95 | ... | N | <3.43 | ... |
| Fe XXIV | Ca XVII | 7.2 | 192.04 | 191.62 | Y | 14.47 | 7.28 |
| Ar XIV | Ca XIV | 6.5 | 194.41 | 193.31 | Y | 5.86 | 3.08 |
| Fe XIV | | 6.3 | 211.33 | ... | N | <4.44 | ... |
| Fe XIV | | 6.3 | 219.13 | ... | N | <4.07 | ... |
| Fe XV | | 6.3 | 243.80 | ... | N | <4.67 | ... |
| Fe XVI | | 6.4 | 251.04 | ... | N | <5.19 | ... |
| Fe XXIV | Fe XVII | 7.2 | 255.10 | 255.10 | Y | 7.68 | 3.15 |
| He II | S XIII | 6.9 | 256.30 | 255.64 | N | <7.68 | ... |
| Fe XVI | Fe XXIII | 6.4 | 262.97 | 262.76 | Y | 5.42 | 2.63 |
| Fe XIV | | 6.3 | 264.78 | ... | N | <4.37 | ... |
| Fe XV | | 6.3 | 284.15 | 284.38 | Y | 13.27 | 6.04 |
| Ni XVIII | | 6.5 | 292.00 | ... | N | <4.91 | ... |
| He II | Si XI | 6.6 | 303.91 | 303.87 | N | 77.68 | 16.50 |
| Fe XVI | | 6.4 | 335.41 | 334.94 | Y | 41.54 | 13.86 |
| Fe XVI | | 6.4 | 360.80 | 359.68 | Y | 21.18 | 7.96 |

Table 3. HD 35850: Derived and Published Parameters

| Parameter | Value | Reference |
|------------------|---|-----------------------------|
| MK | F8–9 V | Cutispoto et al. 1995 |
| d | 26.84 ± 0.62 pc | Perryman et al. 1997 |
| t_{\star} | 10^8 yr | Tagliaferri et al. 1994 |
| V | 6.300 ± 0.006 | Perryman et al. 1997 |
| $B - V$ | 0.553 ± 0.007 | Perryman et al. 1997 |
| M | $1.15M_{\odot}$ | Kim & Demarque 1996 |
| τ_c | 20.7 d | Kim & Demarque 1996 |
| L_{bol} | 6.64×10^{33} ergs s $^{-1}$ | Blackwell & Lynas-Gray 1994 |
| R_{\star} | $1.18R_{\odot}$ | Blackwell & Lynas-Gray 1994 |
| $v \sin i$ | 50 km s $^{-1}$ | Tagliaferri et al. 1994 |
| P_{rot} | 1.40 ± 0.20 d | ... |
| Ro^{-1} | 14.8 ± 2.4 | ... |
| L_X | 1.54×10^{30} ergs s $^{-1}$ | ... |
| R_X | 2.3×10^{-4} | ... |
| F_X | 1.8×10^7 ergs cm $^{-2}$ s $^{-1}$ | ... |
| N_{H} | $1.7_{-1.1}^{+0.3} \times 10^{18}$ cm $^{-2}$ | ... |
| Z | $1.15_{-0.35}^{+0.75}$ | ... |
| T_1 | $6.3_{-2.3}^{+1.6}$ MK | ... |
| Em_1 | 2.8×10^{52} cm $^{-3}$ | ... |
| T_2 | $25.1_{-5.2}^{+6.5}$ MK | ... |
| Em_2 | 4.0×10^{52} cm $^{-3}$ | ... |